Supersonic Propulsive Divert Maneuvers for Future Robotic and Human Mars Missions

Amit B. Mandalia[1] and Robert D. Braun[2]
Georgia Institute of Technology, Atlanta, Georgia, 30332

Future robotic and human missions to Mars require improved landed precision and increased payload mass. Two architectures that seek to meet these requirements using supersonic propulsive diverts are proposed in this paper: one utilizing a high-altitude propulsive divert and another with thrust vectoring during supersonic retropropulsion. Low ballistic coefficient entry vehicles decelerate high in the thin Mars atmosphere and may be used to deliver higher-mass payloads to the surface. A high-altitude supersonic propulsive divert maneuver is proposed as a means of precision landing for low ballistic coefficient entry vehicles that decelerate to supersonic speeds at altitudes of 20-60 km. This divert maneuver compares favorably to state-of-the-art precision landing architectures with range accuracy on the order of 100 m while saving over 30% in propellant mass. Architectures which utilize hypersonic vehicles with ballistic coefficients of 10 kg/m^2 can possibly land within 500 m of a target with this maneuver alone. Supersonic retropropulsion has also been proposed as a means to deliver higher-mass payloads to the surface, and thrust vectoring during supersonic retropropulsion can save a substantial amount of fuel in a precision landing scenario. Propellant mass savings greater than 30% are possible if thrust vectoring is unconstrained during the supersonic phase of flight.

Nomenclature

A	=	Axial force
α	=	Angle-of-attack
β	=	Ballistic coefficient, kg/m^2
C	=	Aerodynamic coefficient
CI	=	Confidence Interval
ΔV	=	Change in velocity, m/s
D	=	Diameter, m
DoF	=	Degree-of-freedom
γ	=	Flight-path angle, defined as positive above the horizon, °
h_0	=	Initial altitude, km
L/D	=	Lift-to-drag ratio
m_0	=	Initial mass, kg
m_{prop}	=	Propellant mass, kg
N	=	Normal Force
θ	=	Off-velocity thrust angle, °
T/W	=	Thrust to Weight, referenced to Mars
V	=	Velocity, m/s

[1] Graduate Research Assistant, Guggenheim School of Aerospace Engineering, Georgia Institute of Technology, AIAA Student Member, a.mandalia@gatech.edu

[2] David and Andrew Lewis Professor of Space Technology, Guggenheim School of Aerospace Engineering, Georgia Institute of Technology, AIAA Fellow, robert.braun@ae.gatech.edu

I. Introduction

FUTURE Mars missions will require improved landed accuracy to safely access areas of scientific interest and strategically place infrastructure for human missions. Also, to increase scientific return and potentially land humans on Mars, larger landed masses are required.[1] Large masses are difficult to land on Mars due to the thin atmosphere which limits aerodynamic deceleration during entry, descent, and landing (EDL). Improved accuracy and landed mass have received significant attention in the past 10 years.[2,3] Inflatable aerodynamic decelerators (IADs) can allow for greater landed mass and supersonic retropropulsion (SRP) has been shown to be an enabling technology for human missions.[4] Current efforts to increase landed accuracy are focused on hypersonic entry and propulsive terminal descent. Guided hypersonic entry, which was successfully demonstrated at Mars for the first time on the Mars Science Laboratory (MSL) mission in 2012,[5] improved landing accuracy substantially in comparison to previous missions. Future landing architectures further propose landing accuracy improvements by employing fuel-optimal algorithms[6] for propulsive descent from the end of parachute flight to a targeted landing site.[7] The state-of-the-art EDL architecture at Mars, with these elements, is shown in Figure 1.
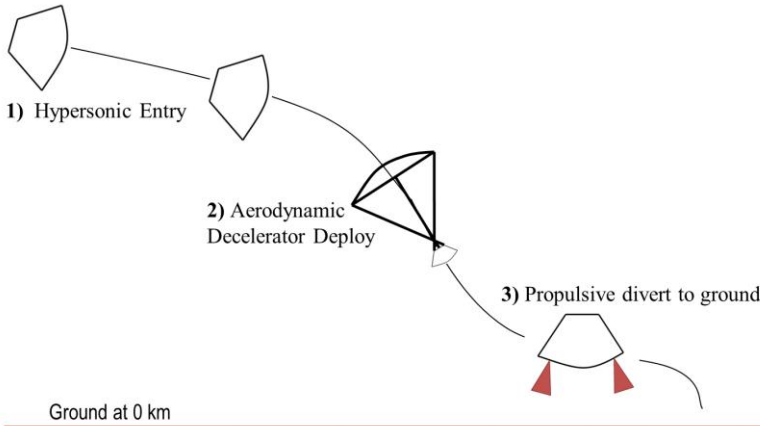

Figure 1. Traditional Entry, Descent, and Landing Architecture at Mars.

To increase the landed payload mass, it is paramount to ensure that the mass of propellant used is minimized. Fuel-optimal algorithms used during propulsive landing attempt to do this, but since these maneuvers are initiated at low altitudes, large diverts with shallow glideslopes require relatively large propellant mass fractions.[8] Beginning propulsive diverts earlier in the trajectory may reduce propellant usage and provide more altitude and timeline during landing.

Low ballistic coefficient vehicles, such as those that use hypersonic IADs (HIADs), have been shown to decelerate much higher in the atmosphere at Mars, between 20 and 60 km.[9] This allows for more time of flight between the end of hypersonic flight and the point of parachute deployment at 6-10 km. For the first part of this study, it is postulated that performing propulsive maneuvers during this high-altitude portion of flight to target a landing site will lead to an overall reduced propellant usage and a precision landing capability. By thrusting orthogonal to the velocity vector, all energy would be put into a divert to a target during the maneuver.

The second phase of the study explores the use of thrust vectoring during supersonic propulsive descent (supersonic retropropulsion) to accomplish a divert. Current SRP studies have evaluated thrusting directly opposite the velocity,[4] but it is postulated that thrust vectoring can allow for efficient fuel use in a precision landing scenario. The higher velocities and altitude of such a maneuver might allow for greater diverts at decreased propellant costs relative to a divert that begins during subsonic flight. Table 1 summarizes guidance techniques that can be used to decrease landing error at Mars, where the shaded items are those investigated here. The proposed maneuvers fill a gap for crossrange control and active downrange control during the descent phase of flight. Precision landing is defined by the mission requirements, as a human mission may require meter-level accuracy, while a science mission may require a 1 km accuracy, so the term will be used loosely as landing with some degree of targeting accuracy.

Table 1. Summary of in-flight precision landing techniques for Mars exploration missions.

	Deceleration Device	Crossrange control	Downrange control
Entry	Aeroshell (Rigid/Inflatable)	Bank-to-Steer	
Descent	Aerodynamic Decelerator (Rigid / Inflatable / Parachute)	Bank-to-Steer	
		None	Range Trigger
		Propulsive Divert Maneuver?	
	Supersonic Retropropulsion	Thrust Vector?	
Landing	Propulsive	Thrust Vector	
	Subsonic Parachute	Guided Parachute	
	Impact Attenuation	None	

II. Simulation Methods and Assumptions

A. Numerical Simulation

To perform high-fidelity simulations for the conceptual studies described in this paper, architectures were catalyzed through a three degree-of-freedom simulation. This simulation models the planet as a rotating oblate spheroid, and includes higher-order effects such as the J2 perturbation. The equations of motion are integrated with a constant timestep 4th order Runge-Kutta integration scheme in a planet-centered inertial frame. It is written in MATLAB, but autocoded to C to improve execution speed. Versions of this simulation have been validated and used in previous design studies.[10]

A simulated flight computer allows for the operation of navigation, guidance, and control at different rates. The simulation ends when the vehicle lands at the target altitude, initially set at 0 km. The simulation is run at a rate of 50 Hz, with guidance calls at 10 Hz. Perfect navigation (full state knowledge) is assumed for this simulation.

B. Planetary Models

Atmospheres were generated using Mars-GRAM 2010,[11] and correspond to an August 6, 2012 landing date (MSL's landing date) using default Mars-GRAM settings. A dust tau of 0.3 was used for these atmospheres. A nominal atmosphere without winds is used for the nominal performance and sensitivity analysis. For the Monte Carlo analyses, a set of 1000 dispersed atmospheres with winds were generated. This landing date corresponds to a time when the Mars atmosphere is at the lower half of its pressure cycle, thereby representing a conservative set of atmospheres in comparison to other times of the Martian year. Other parameters used to characterize Mars in the simulation are found in Table 2.

Table 2. Properties of Mars.

Property	Value
Equatorial Radius	3396.2 km
Polar Radius	3376.2 km
Gravitational Parameter, μ	4.283×10^{13} m^3 / s^2
J2 Perturbation	1.9605×10^{-3}
Ratio of Specific Heats	1.294
Sutton-Graves Coefficient	1.898×10^{-4} kg$^{0.5}$/m

C. Vehicle Models

Aerodynamic models are used for the aeroshell and the parachute. A MSL-class 3300 kg vehicle is modeled, with a 4.5-m diameter 70° sphere-cone forebody with a nose radius of 1.125 m. Only C_A and C_N are modeled, with bank angle tracked to point the lift vector in the correct direction. For an MSL lifting entry at α_{tot} = -16° and ballistic α_{tot} = 0°, an existing aerodynamic database was used. A disk-gap-band parachute with D_o = 19.7 m was used in the simulations, using a historical aerodynamic database.[12]

Engines are modeled as force vectors that can point in any direction, restricted by minimum and maximum thrust magnitudes. Restrictions on the thrust pointing are specific to the configurations conceptualized below. Hydrazine thrusters (Isp = 225 s) were used for the high-altitude divert maneuver study and methane-LOx engines (Isp = 350 s) were used for the SRP study.

D. Entry State

An MSL-like entry state[9] was used unless otherwise stated. This allowed for parity to compare results and also make sure realistic dispersions were used. The target was always at an altitude of 0 km and the latitude/longitude of the target depended on the scenario.

Table 3. Entry state for simulations.

Entry State	Value
Inertial Flight-Path Angle, γ	-15.5°
Inertial Entry Velocity	6.1 km/s
Azimuth	90°
Entry Interface (EI) Altitude	135 km
EI Latitude	0°
EI Longitude	0°

3

E. Monte Carlo Dispersions

The dispersions used in the Monte Carlo Simulation are found in Table 4, along with their references. Entry state delivery errors are correlated from a MSL delivery covariance matrix.[9]

Table 4. Monte Carlo Dispersions

	Parameter	Dispersion, Min/Max or 3σ	Reference
Entry State	Inertial Flight-Path Angle, ɣ	0.05°	Gaussian, Ref. 9
	Inertial Entry Velocity	2.0 m/s	Gaussian, Ref. 9
	Azimuth	0.005°	Gaussian, Ref. 9
	Entry Interface (EI) Altitude	2.5 km	Gaussian, Ref. 9
	EI Latitude	0.1°	Gaussian, Ref. 9
	EI Longitude	0.1°	Gaussian, Ref. 9
	Vehicle mass	3.0 kg	Gaussian, Ref. 9
Vehicle	Hypersonic C_A	3%	Uniform, Ref. 13
	Hypersonic C_N	10%	Uniform, Ref. 13
	Supersonic C_A	5%	Uniform, Ref. 13
	Supersonic C_N	8%	Uniform, Ref. 13
	Parachute Aerodynamics	From literature	Ref. 12
Planetary	Atmosphere	Generated in Mars-GRAM	Described above

III.   High-Altitude Divert Architecture

A. Conceptual Description

The high-altitude divert maneuver can be thought of as a modification to powered descent. Typical powered descent methods use a single thrust vector to provide both deceleration and divert capabilities. The idea behind the high-altitude divert maneuver is to still use terminal powered descent for deceleration and soft landing, but decouple the divert function and perform it earlier in the trajectory. It is postulated that this decoupling, accomplished by applying thrust normal to the velocity vector, can substantially reduce fuel usage. This thrust implementation allows for possible use of a lifting aerodynamic effector (in lieu of the thruster) and minimizes the total effect of the maneuver on the velocity to prevent excessive acceleration during maneuvers.

B. Architecture Detail

The architecture that will be analyzed utilizes a hypersonic entry with a rigid heatshield or HIAD, a propulsive divert maneuver at high-altitudes, parachute flight for further deceleration, and a constant thrust propulsive gravity turn for a soft landing. The Mars-relative thrust-to-weight is constrained to be less than 0.5 in each direction (in-plane and out-of-plane) for the divert maneuver, and T/W = [2-5] (relative to Mars) for the gravity turn. A jettison Mach number for a given mission type is selected to ensure the nominal trajectory passes through the center of the parachute deployment box. Parachute deployment at 6-10 km allows for a relatively wide range of deploy conditions for a disk-gap-band (DGB) parachute on Mars, while still preserving altitude.[1] A propulsive gravity turn to the ground allows for the targeting performance of high-altitude divert maneuver to be examined with minimal external guidance influences. It also completes the decoupling of the propulsive maneuvers, where thrust for the gravity turn is only applied to decelerate the vehicle. Figure 2 shows this architecture in detail.
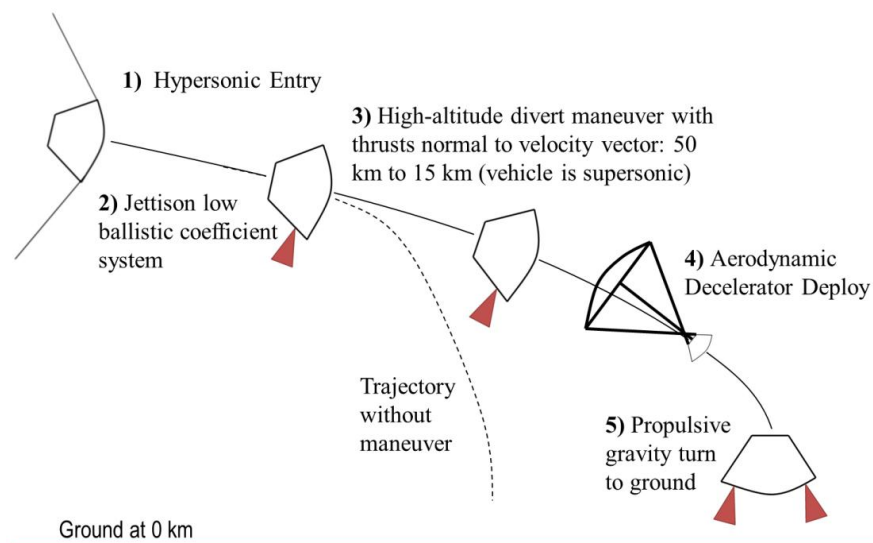
4

Figure 2. Architecture with high-altitude divert maneuver.

C. High-Altitude Divert Guidance

The guidance algorithm for the high-altitude divert maneuver consists of a closed-loop prediction-based algorithm. The algorithm propagates simplified equations of motion for the current trajectory to identify the vehicle's zero-effort landing location. The target is projected on the current plane of motion and compared to the zero-effort landing location to obtain the downrange miss distance. The magnitude of this projection off-the-plane allows for the calculation of the crossrange miss distance.

With knowledge of the miss distances, thrust can be commanded to reach the target. As discussed earlier, the thrust is applied normal to the velocity vector. For downrange control, if vehicle is determined to be missing the target, thrust is commanded to force the vehicle to follow a trajectory toward a target in the current plane of motion. For crossrange control, thrust is commanded out-of-plane in the direction of the target. The closed loop implementation turns off the engine as soon as the predictor determines the zero-effort landing location has converged on the target. This is described in further detail in Figure 3.
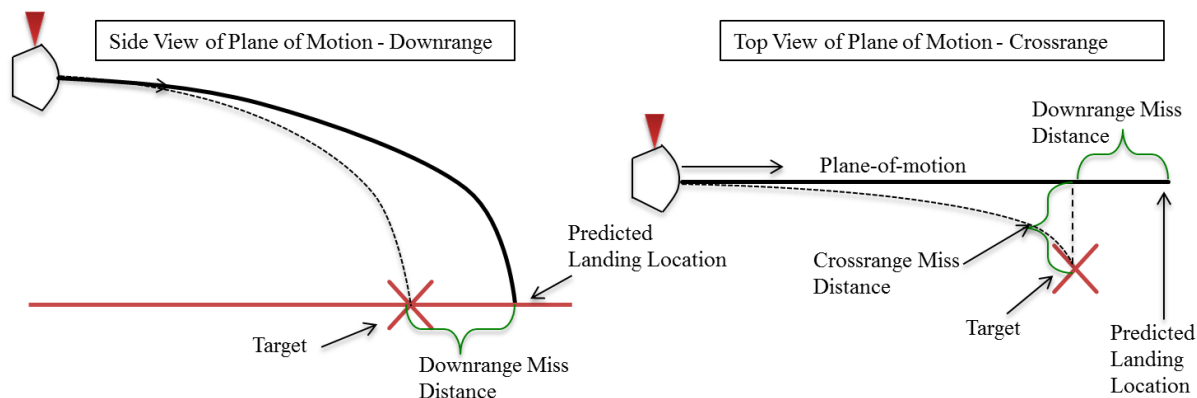

Figure 3. Description of high-altitude divert maneuver guidance strategy. In-plane thrusts are shown controlling downrange in the left image, and out-of-plane thrusts are shown controlling cross range in the right image.

D. Architecture Performance

1. Baseline Vehicle and Mission

To understand results of the maneuver, a modified Mars Science Laboratory (MSL)[14] vehicle was simulated. In order to accommodate this maneuver, pairs of Mars Landing Engines (MLEs) were spaced 90° apart on the plane normal to the velocity vector. This corresponds to a Mars-relative T/W = 0.5 in each channel. For the divert

5

maneuver, the 3300 kg vehicle is assumed to be traveling at 0° angle-of-attack with the MLEs acting through the center of gravity. This configuration can be seen in Figure 4.
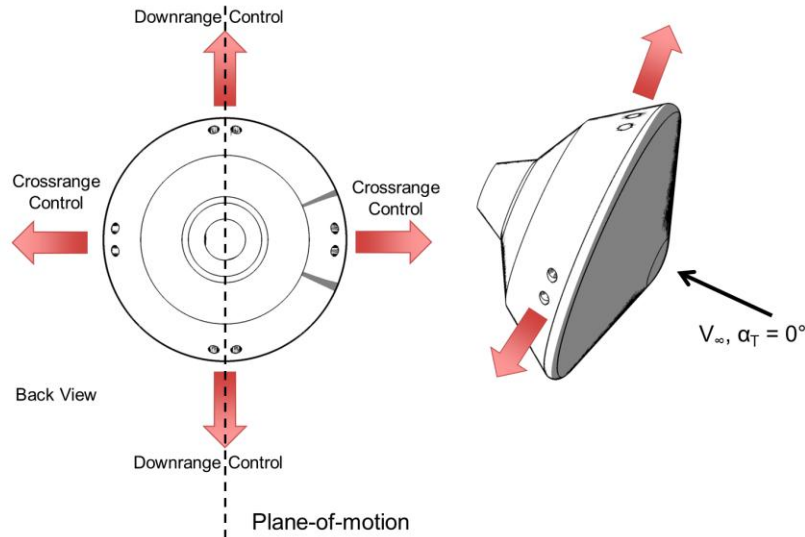

Figure 4. Configuration of vehicle with the high-altitude divert thrusters.

Vehicles with hypersonic ballistic coefficients of 1 kg/m^2, 5 kg/m^2, 10 kg/m^2, 20 kg/m^2, 50 kg/m^2, which enter ballistically, were simulated as part of this study, where ballistic coefficient is defined as m_{entry} / (C_DA). The hypersonic trajectories are based on the work of Meginnis et al.[9] The ballistic coefficients are varied with the addition of a HIAD to the system, whose mass is estimated using relationships from the literature.[15] The total entry mass is the mass of the HIAD plus 3300 kg. Table 5 lists the vehicle properties for the different vehicles. Trajectories are shown in Figure 5, where the hypersonic entry, high-altitude divert maneuver, flight on parachute, and propulsive gravity turn, are all modeled. The only mass changes modeled are HIAD jettison and propellant usage from propulsive maneuvering. At the point of HIAD jettison, the drag area is reduced to that of the MSL blunt body and the mass of the HIAD is subtracted. Also, if more precise navigation data is desired, a terrain-relative navigation (TRN) or radar sensor can be exposed during a jettison event.

Table 5. Low-β vehicle properties. Masses are estimated from known relationships.[15]

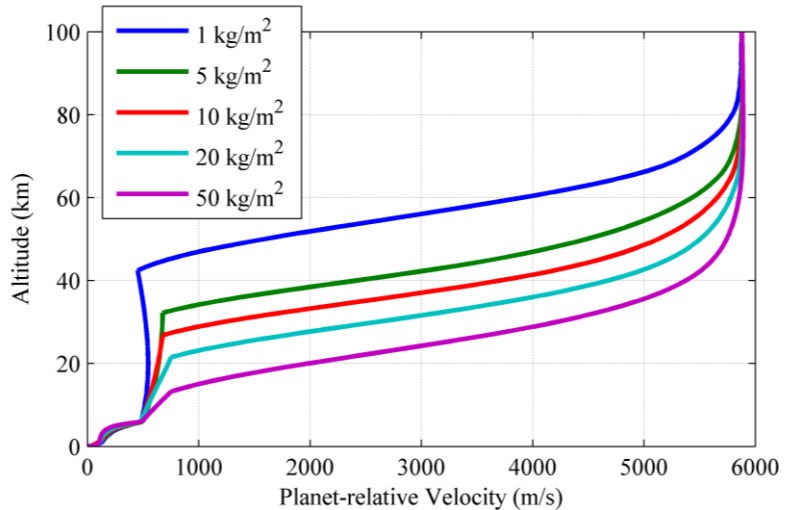| β (kg/m^2)	HIAD Diameter	HIAD Mass
1	56 m	500 kg
5	24 m	174 kg
10	17 m	83 kg
20	11.9 m	43 kg
50	7.5 m	27 kg

Figure 5. Low-β vehicle trajectories.

For all the trajectories, the jettison of the HIAD occurs at relatively low velocities. The jettison event appears as the discontinuity at 42 km, 33 km, 27 km, 22 km, and 16 km, for the 1 kg/m^2, 5 kg/m^2, 10 kg/m^2, 50 kg/m^2 trajectories in Figure 5, respectively. After that, a 3300 kg, β = 148 kg/m^2 vehicle at 0° angle-of-attack is released, and the divert maneuver is allowed to begin. For the 1 kg/m^2 case, the atmosphere is not dense enough at the high altitudes, so the vehicle initially accelerates, unlike the other trajectories, which continue decelerating after jettison.

The jettison is commanded on a velocity trigger, and the velocities are chosen so that the post-jettison trajectory would fall through the center of the Disk-Gap-Band parachute deployment box. A range trigger may allow for further downrange control, but this would compete with this guidance of this maneuver and was therefore not implemented. Mach, velocity, dynamic pressure at jettison, and maximum dynamic pressure for the nominal trajectories are found in Table 6. Jettison occurs after the dynamic pressure pulse, and since dynamic pressure at jettison is far lower than maximum dynamic pressure for the entire trajectory, it is likely that effects of aerodynamic and atmospheric uncertainties will be minimized.

Table 6. Nominal trajectory parameters at jettison, including maximum dynamic pressure.

β (kg/m^2)	Jettison Velocity (m/s)	Mach Number at Jettison	Dynamic Pressure at Jettison (Pa)	Maximum Dynamic Pressure (Pa)
1	450	2.406	12.98	180.8
5	675	3.491	122.4	754.5
10	675	3.381	229.2	1553
20	750	3.622	501.2	2979
50	750	3.417	1115	6780

Aerodynamic, wind, and atmospheric uncertainties are directly dealt with using thrust during the high-altitude divert maneuver, but after parachute deploy, these uncertainties act more strongly on the vehicle and there is no active guidance to prevent it's influence. It is anticipated that the greatest range error will be accumulated after parachute deployment.

2. Statistical Performance

Statistical performance of this maneuver is analyzed using a Monte Carlo simulation. One-thousand trajectories of β ∈ {1 kg/m^2, 5 kg/m^2, 10 kg/m^2, 20 kg/m^2, 50 kg/m^2} each with a gravity turn only (unguided), state-of-the-art propulsive landing initiated at Mach 0.8, and the high-altitude divert maneuver were run. The mean latitude and longitude of the gravity turn cases were set as the target for the state-of-the-art propulsive landing cases, while a target about 5 km further downrange was set for the high-altitude divert maneuver, in order to capitalize on the lift-modulation like characteristics of the high-altitude diver maneuver. The results of these 15 sets of runs are shown in the following figures. In the cumulative probability density function for PMF (Figure 6), the high-altitude divert maneuver is 60-70% more expensive in PMF than the gravity turn by itself, while the state-of-the-art propulsive landing is upwards of 200% more expensive. The state-of-the-art propulsive landing PMFs are not consistent through the cumulative distribution, since the result is highly sensitive to initial conditions, but the 99% CI PMF (between 0.27 and 0.32) is consistently higher than the other architectures.
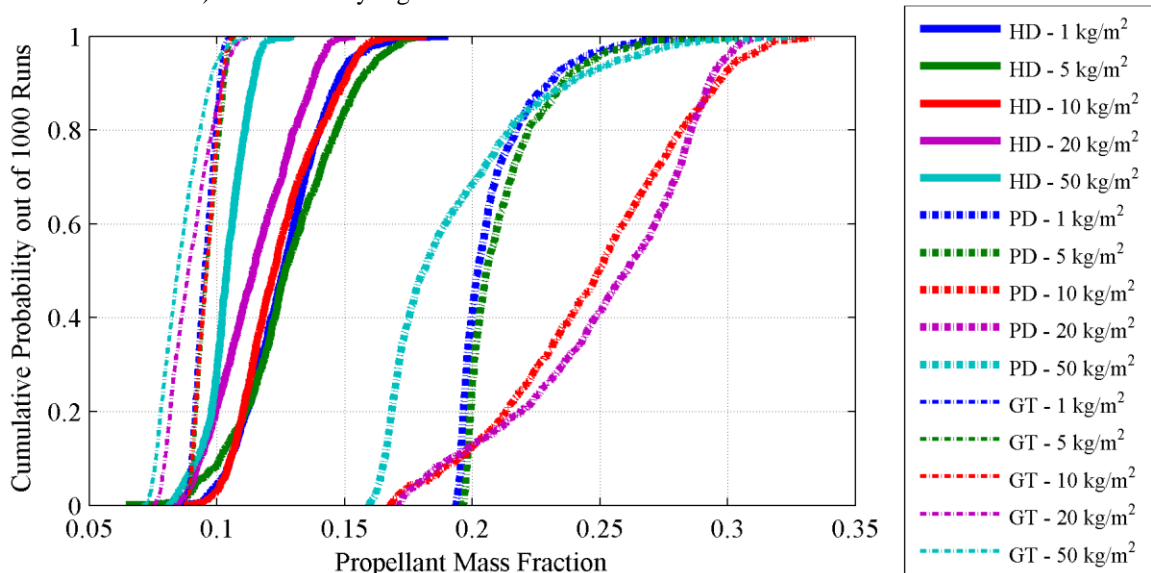

Figure 6. Cumulative Probability Function of PMF for all 15 architectures. HD is the high-altitude divert, PD is the state-of-the-art propulsive descent, and GT is the gravity turn alone.

7

The 99% confidence level results for all the CDF's are summarized in Table 7. The results shaded in grey refer to mission types that were able to land within 500 m. The column PMF Reduction quantifies the percent difference between the high-altitude divert PMF and state-of-the-art propulsive landing PMF. Across all cases, the high-altitude divert maneuver uses at least 37% less propellant compared to the state-of-the-art propulsive landing case.

Table 7. 99% confidence statistics for Monte Carlo study.

β (kg/m^2)	Unguided (Gravity turn only): 99% CI		High-Altitude Divert Maneuver: 99% CI		State-of-the-art propulsive Landing: 99% CI		PMF Reduction
	PMF	Miss Distance (m)	PMF	Miss Distance (m)	PMF	Miss Distance (m)	
1	0.104	17000	0.173	201	0.278	0.7	-37.7%
5	0.106	14400	0.177	356	0.288	0.8	-38.5%
10	0.106	12000	0.164	494	0.328	39	-50%
20	0.111	13300	0.148	6200	0.310	57	-52.2%
50	0.111	15600	0.123	9800	0.301	11	-59.1%

Although the high-altitude divert maneuver's PMF performance is far better than state-of-the-art propulsive landings' PMF, the uncontrolled region past parachute deploy causes the vehicle to miss by several hundred meters for the most precise cases (Figure 7). This is compared to state-of-the-art propulsive landing, which is able to land within a few meters of the target. If a 500 m miss distance is deemed to be acceptable for a mission, it can be said that high-altitude divert architectures of this type with $\beta \leq 10$ kg/m^2 should be able to achieve this landing requirement, possibly without the need for entry guidance. Targeting performance degrades when $\beta \geq 20$ kg/m^2, as altitude and timeline to perform the divert maneuver decrease at the higher ballistic coefficients.
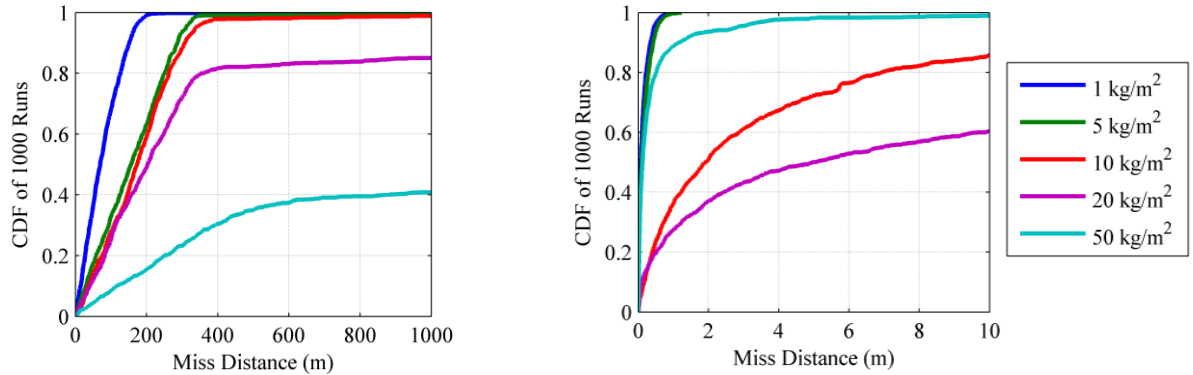

Figure 7. CDF's of miss distance for the high-altitude divert (left) and the state-of-the-art propulsive landing (right).

The altitude verse crossrange for each of the 1000 trajectories for the $\beta = 5$ kg/m^2 mission are shown in Figure 8. for the high-altitude divert and Figure 9 for the state-of-the-art propulsive landing architecture. For the high-altitude divert, downrange error is clearly decreased during the high-altitude maneuver, while the state-of-the-art propulsive landing waits until the last few km of altitude to begin a large divert (often over 10 km). It was postulated that there were PMF advantages to starting a divert at higher altitudes compared to a shallow glideslope state-of-the-art propulsive landing, and this is confirmed by the results in Table 7.
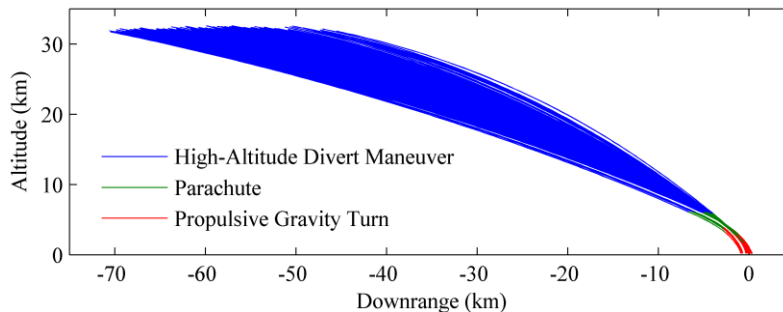

Figure 8. Altitude verse downrange for the high-altitude divert architecture.
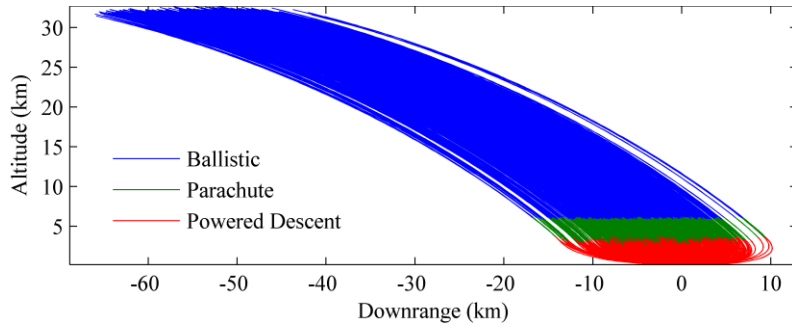
8

Figure 9. Altitude verse downrange for the state-of-the-art propulsive landing architecture.

A plot of the 1000 crossrange verse downrange trajectories for the high-altitude divert maneuver (β = 5 kg/m^2 mission) can be found in Figure 10. The heading change for all trajectories happens quickly, soon after the initiation of the divert maneuver and far uprange (over 40 km) away from the target. Likewise, the maneuver is able to control crossrange on the order of meters. This is in comparison to the crossrange verse downrange trajectories for the state-of-the-art propulsive landing architecture, shown in Figure 11, where powered descent flight is shown (the only precision guided part of flight). The initial crossrange error is increased in comparison to the high-altitude divert, as the propulsive landing divert starts at a lower altitude allowing aerodynamic and wind uncertainties to have more opportunity to act on the vehicle. However, the state-of-the-art propulsive landing is capable in reducing the range error, including the downrange error seen in Figure 9, down to 0.8 m at 99% CI (Table 7).
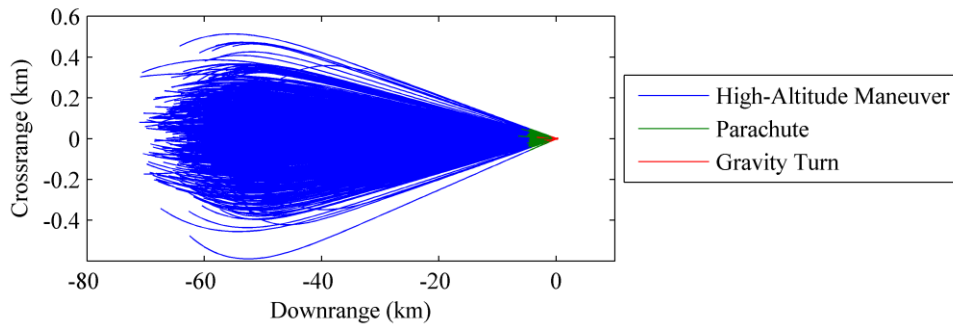

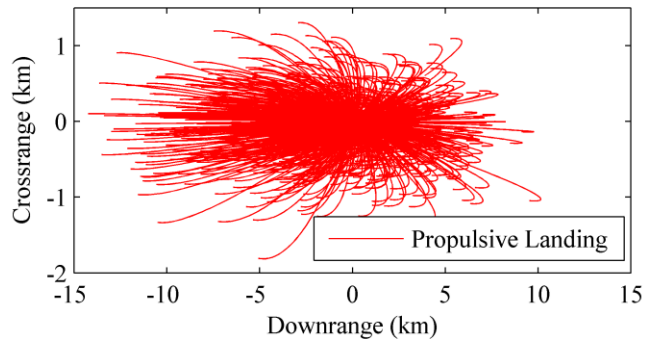**Figure 10. Crossrange verse downrange for the high-altitude divert maneuver.**

Figure 11. Crossrange verse downrange for the state-of-the-art propulsive landing (only powered descent flight is shown).

To get a better idea of the as-landed performance of the architectures, the touchdown locations for the 1000 samples from the Monte Carlo simulations of the β = 5 kg/m^2 mission are reported in Figure 12. Note that the high-altitude divert maneuver's landed positions are further downrange than the state-of-the-art propulsive landing target since it's target was chosen to be further downrange. Compared to the unguided ellipse, the crossrange error is reduced to near zero when using the state-of-the-art propulsive landing and the high-altitude divert maneuver (indicated by almost no variation in crossrange). The high-altitude divert maneuver is also capable of reducing the downrange error by a factor of 10 compared to the unguided landing ellipse, while the state-of-the-art propulsive

9

landing reduces downrange to near zero. The actual miss distances from the target for the $\beta = 5$ kg/m^2 missions are documented by the green CDF curves in Figure 7.
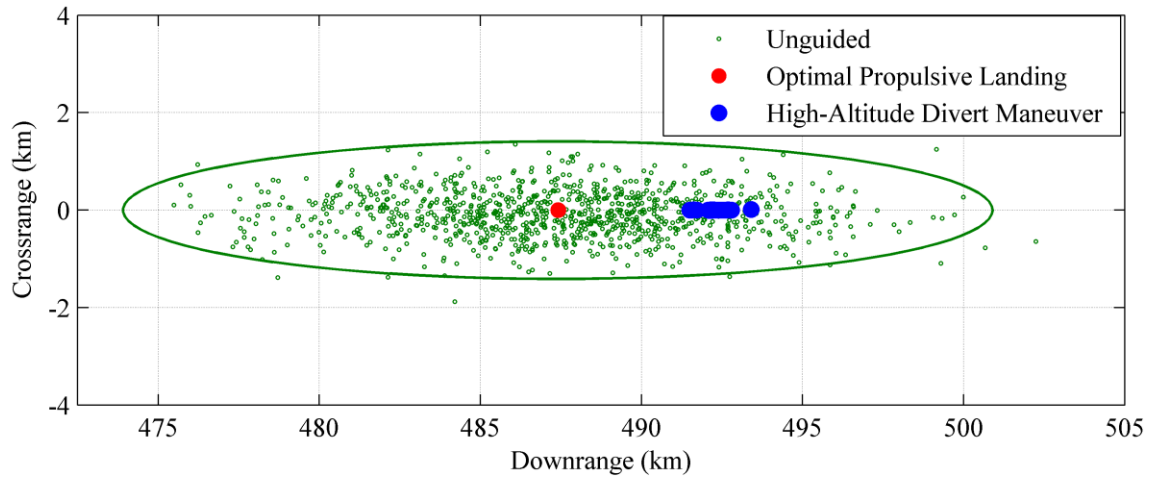

Figure 12. Touchdown locations for the $\beta = 5$ kg/m^2 architectures, with a landing ellipse drawn for the unguided cases. The touchdown locations at 0 km altitude of the 1000 sample Monte Carlo simulation are shown for each architecture.

IV. Supersonic Retropropulsion Divert Architecture

A. Conceptual Description

Past entry architectures that have conceptualized using supersonic retropropulsion use it purely as a decelerator in the supersonic regime. In this manner, thrust is applied directly against the velocity.[16] With precision landing becoming an increasingly more important requirement, it is postulated that performing divert maneuvers during this phase may be beneficial. Current state-of-the-art propulsive descent guidance use optimal control techniques to divert to a landing site. To date propulsive guidance has only been investigated in the subsonic flight regime[8] and current entry architectures have used supersonic retropropulsion only for deceleration. By expanding the start of propulsive descent guidance into the supersonic regime, both deceleration and a targeted divert can be achieved by supersonic retroproplusion. Using the results from the previously described architecture, it is postulated that diverts at higher velocities and altitudes will more efficiently use fuel to achieve landing goals. These diverts are accomplished with thrust vectoring during the supersonic phase of flight.

B. Architecture Detail

The vectored-thrust supersonic retropropulsion architecture is described in detail in Figure 13. The angle θ is defined as the off-velocity thrust angle, which can be constrained relative to the velocity vector that the thrust can vector, while the vehicle is supersonic. This is a practical constraint, similar to angle-of-attack, that is set by aerodynamic limitations (the vehicle is stable at certain angle-of-attacks, for example) and navigation sensor viewing constraints. Existing SRP studies assume propulsive gravity turn laws during the SRP burn, where $\theta = 0°$ throughout the entire trajectory.[4,17] For this architecture, as soon as the vehicle passes into the subsonic regime, thrust vectoring is unconstrained until touchdown. If increased navigation accuracy is desired, the transition between hypersonic entry and SRP initiation may allow for the exposing of a TRN or radar sensor while the engines are being exposed.
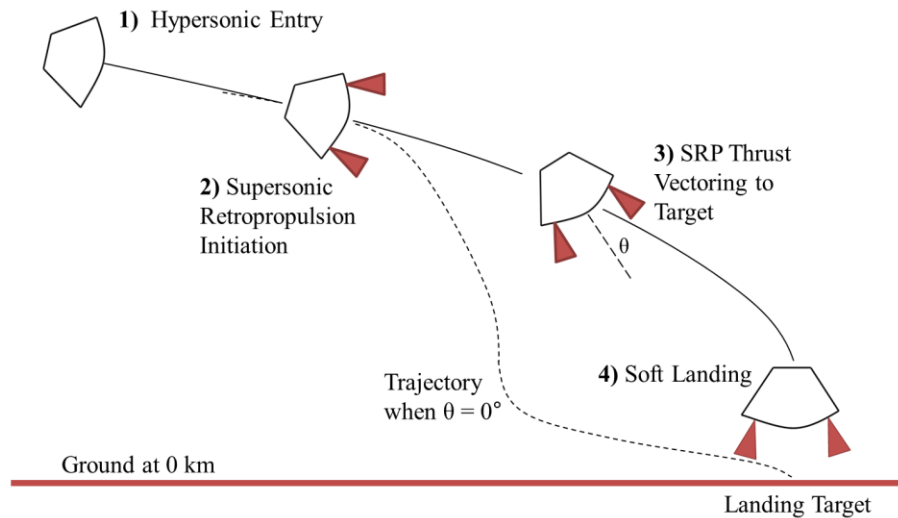
10

Figure 13. Architecture with thrust vectoring during SRP.

C. Supersonic Retropropulsion Guidance and Implementation Strategy

The optimal propulsive guidance law from the previous architecture study is used.[8] This is an analytic, acceleration-optimal guidance law, that uses a Lagrange multiplier approach to determine acceleration commands. At every guidance call, run at 10 Hz, the algorithm determines an acceleration vector. The optimal propulsive trajectory is verified within the algorithm to make sure that the trajectory is feasible (trajectory does not pass through the ground). If it is in violation, a weighting on time-to-go is increased, until the algorithm finds a trajectory that meets the constraints. The acceleration is constrained to the maximum and minimum thrust capability of the system. If the vehicle is supersonic, the off-velocity thrust angle is checked to make sure it satisfies a prescribed angle constraint. If exceeded, the thrust vector is rotated on the velocity-thrust vector plane to the angle constraint.

1. Glideslope constraint

A common feature of optimal propulsive descent trajectories is fast-moving, but low altitude flight. This often causes a >100 m/s glide a few hundred meters off the ground, often ending in a high-velocity impact during the simulation. In order to mitigate these events, a 20° glideslope constraint is applied when the vehicle is farther than 750 m away from the landing site.

This glideslope constraint is not handled by the optimal landing law, so a different propulsive landing law was used in this situation. At the point where the vehicle violates the glideslope, a trajectory based on a polynomial law is created towards the target. Since the vehicle cannot instaneously transition into this trajectory, a feedback linearization control law is used to allow the vehicle to safely transition and follow the new trajectory. Although not fuel-optimal, it is able to create flight-realistic trajectories.

2. Range Trigger (SRP Initiation Mach Number)

The guidance law is unable to determine a Mach number to initiate SRP. This is important, since it may be more efficient to initiate earlier or later, depending on how far downrange the target is relative to the vehicle. To account for this, the initiation Mach number is kept as a free variable in the simulation. A function for the propellant mass fraction is created, where PMF = f(SRP initiation Mach number). A golden-section search method is used to determine what initiation Mach number produces the minimum PMF. The initiation of SRP at this Mach number tends to act as a range trigger.[18]

D. Simulation Assumptions

Although the same simulation environment is used as the previous study, additional assumptions are made regarding thrust limitations and aerodynamics. Minimum thrust is constrained to 10% of maximum thrust, reflecting deep throttling capabilities. Also, the thrust vector is allowed to change direction instantaneously. This assumption was found to be valid because the tested trajectories usually had continuous thrust movement, except when the thrust angle constraint is changed during flight. When the vehicle is supersonic, the off-velocity thrust angle is limited to a

prescribed angle (effectively angle-of-attack), but as soon as the vehicle is subsonic, this angle is unconstrained. Aerodynamic forces are ignored while the vehicle is thrusting.

E. Vehicle Description

In an effort to understand results of the maneuver, a modified Mars Science Laboratory[19] vehicle is simulated. This vehicle is shown in Figure 14. A modified Apollo Final Phase guidance algorithm is used for hypersonic entry, and produces a constant altitude segment between 10 and 20 km, much like was seen in the MSL mission. Methane – LOx engines are used for parity with previous studies.[4] The engines are assumed to be fixed at 0° cant, with thrust vectoring achieved through the use of differential throttling.

Table 8. Vehicle parameters for the SRP thrust vectoring study.

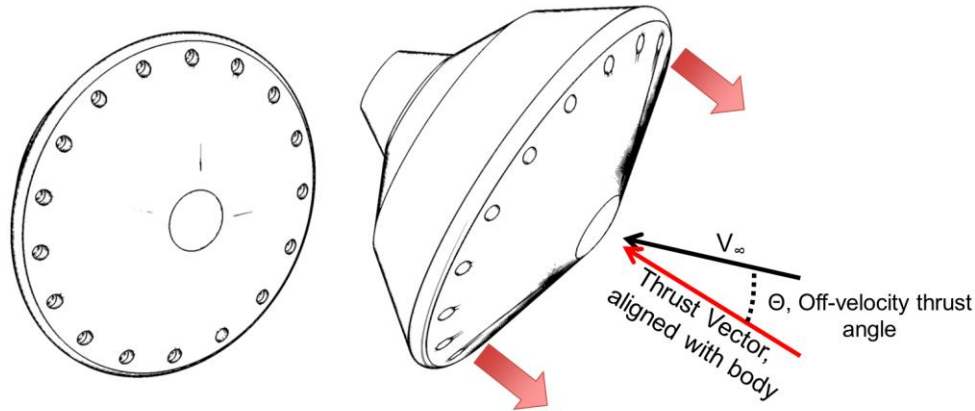| Variable	Vehicle Parameter	Value
Mass		3300 kg
Aerodynamics	Aeroshell	70° sphere-cone, 4.5 m diameter
	L/D	0.24
Engine	T/W (Mars-relative, at start)	5 (~17 MLEs at 0° cant)
	Propellant (Isp (s))	Methane – LOX (350 s)

Figure 14. Configuration conceptualized for use in the SRP study.

F. Architecture Performance

One-thousand runs were performed with appropriate dispersions as found in Table 4, for differing supersonic thrust angle constraints. A single landing target was chosen, based on the center of a landing ellipse of the unguided trajectories. The supersonic thrust angle constraint was varied: 0°, representing a traditional architecture where thrust directly opposes velocity, 10°, 20°, and unconstrained.

1. Propellant Mass Fraction and Miss Distance

Propellant mass fraction and miss distance are reported in cumulative distribution functions in Figure 15, with 99% CI PMF figures in Table 9. Across the board, PMF is decreased as the thrust angle constraint is relaxed, with up to a 32% reduction for the unconstrained case. As the vehicle thrust angle constraint is relaxed, the vehicle is allowed to follow more optimal trajectories, and thus the divert can be handled with less fuel. Although a 10% reduction might be modest for the 10° case, it could amount to few hundred kilograms on large vehicles. This supports the PMF reductions found in the sensitivity studies. Likewise, miss distance at the 99% CI is kept between 50-90 m.

Table 9. 99% confidence for PMF from the Monte Carlo runs.

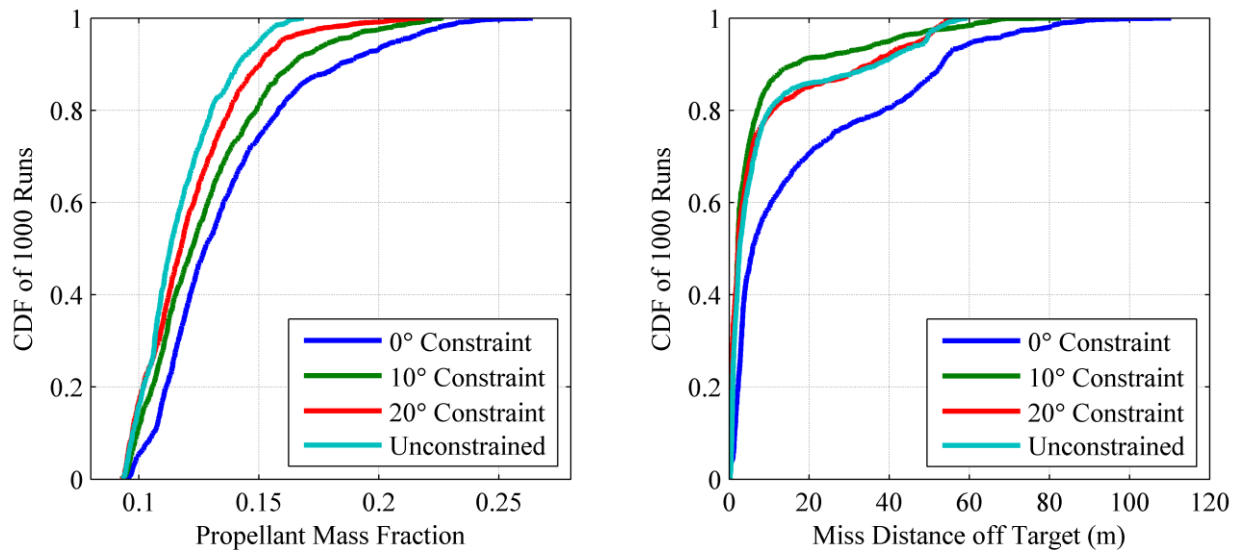|	0° (Traditional)	10°	20°	Unconstrained
99% PMF	0.233	0.214 (10% reduction)	0.199 (16.4% reduction)	0.161 (32.3% reduction)

12

Figure 15. CDF's of PMF (left) and miss distance (right) for Monte Carlo runs with different thrust angle constraints.

Statistics of landing velocity and Mach number at SRP initiation are documented in Figure 16. All cases demonstrate soft landing capability, with all landings under 25 m/s. The deceleration from 25 m/s to 0 m/s can happen quickly with the thrust-to-weight used. The knee at 2 and 5 m/s indicate the trajectories that violated a glideslope constraint, and were forced to follow a polynomial law. Initiation Mach number does not differ much between constraints, except that the unconstrained cases initiate at a slightly lower Mach number. Initiation occurs between Mach 1.3 and 2.1 and is indicative of the golden-search method at work to choose the minimum fuel initation Mach number.
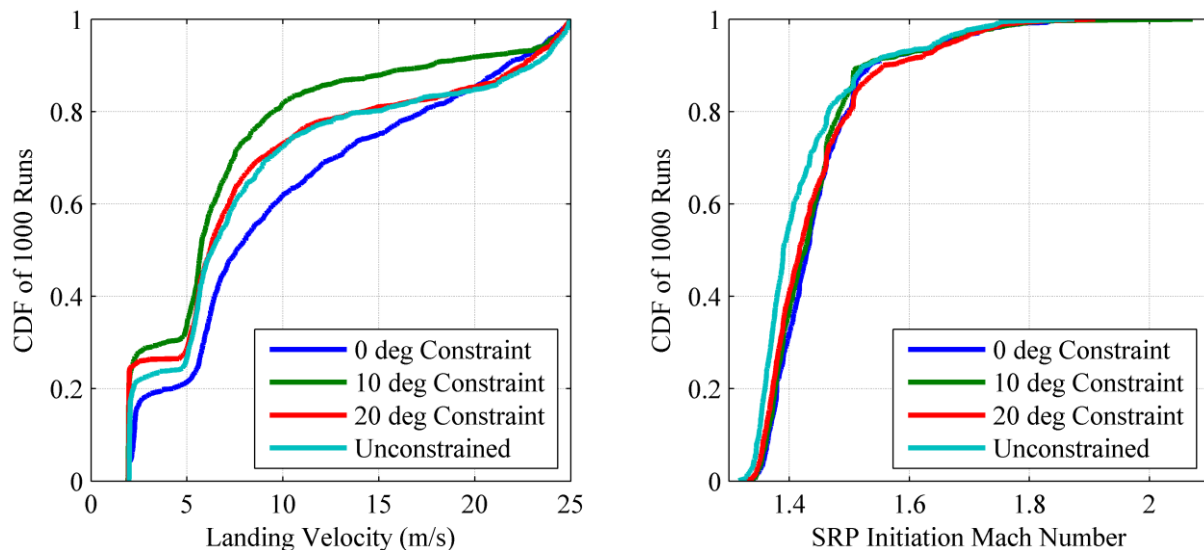

Figure 16. CDF's of landing velocity (left) and SRP initation Mach number for the Monte Carlo runs.

Figure 17 shows the thrust angle behavior throughout supersonic flight. This figure demonstrates that the thrust constraint is active for some of the trajectories. Note for the 0° constrained cases, the 0.16° maximum is within an acceptable tolerance of the constraint. For a few of the unconstrained large diverts, an 80° initial thrust angle may be necessary, but it decreases to about 40° when crossing Mach 1. After initiation, thrust angle does not change much, which means quick maneuvers are not required for diverts during supersonic retropropulsion. Also of interest is the fact that no trajectories favor a 0° thrust angle.
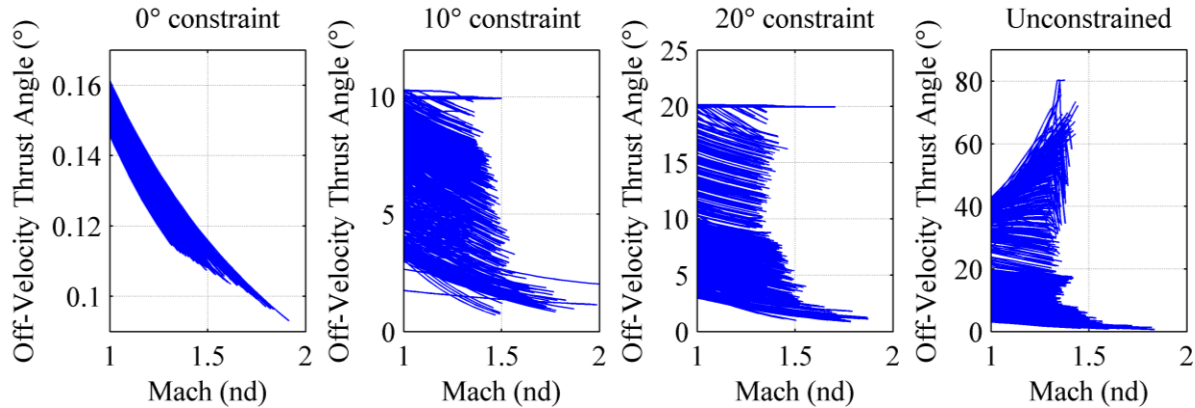
13

Figure 17. Thrust angle vs. Mach from the Monte Carlo runs for different supersonic thrust angle constraints.

V. Conclusions

Two new architectures that utilize supersonic propulsive divert maneuvers have been presented. One is the high-altitude divert maneuver, which leverages altitude margin of low ballistic coefficient vehicles to perform diverts to a target, while the other involves thrust vectoring during supersonic retropropulsion. Expanding the propulsive maneuver envelope into the supersonic regime has been shown to have benefits in both range control and propellant usage efficiency.

The high-altitude divert maneuver was found to enable landing within 500 m for vehicles that enter on a ballistic trajectory with hypersonic $\beta \leq 10$ kg/m^2, without the need for entry guidance. This architecture is over 37% more efficient in propellant mass fraction compared to state-of-the-art propulsive landing architures. Missions that utilize low ballistic coefficient vehicles may benefit from this architecture to decrease landing error and might be able to avoid using guided entry technologies that may be difficult to implement on the vehicle.

Thrust vectoring during supersonic retropropulsion was found to save fuel while achieving pinpoint landing goals. Traditional SRP architectures have utilized thrusts directly opposing the velocity vector, but if the supersonic off-velocity thrust angle is relaxed, savings in propellant mass fraction over 30% are possible, with no loss in landing precision.

VI. Acknowledgments

VII. References

[1] Braun, R. D. and Manning, R. M., "Mars Exploration Entry, Descent, and Landing Challenges," Journal of Spacecraft and Rockets, Vol. 44, No. 2, 2007, pp. 310-323.

[2] Dwyer-Cianciolo, A. M., Davis, J. L., Komar, D. R., Munk, M. M., Samareh, J. A., Powell, R. W., Shidner, J. D., Stanley, D. O., Wilhite, A. W., Kinney, D. J., McGuire, M. K., Arnold, J. O., Howard, A. R., Sostaric, R. R., Studak, J. W., Zumwalt, C. H., Llama, E. G., Casoliva, J., Ivanov, M. C., Clark, I., and Sengupta, A., "Entry, Descent and Landing Systems Analysis Study: Phase 1 Report," Tech. Rep. TM-2010-216720, NASA, July 2010.

[3] Drake, B. G., ed., "Human Exploration of Mars: Design Reference Architecture 5.0", NASA-SP-2009-566, 2009.

[4] Steinfeldt, B., Theisinger, J., Korzun, A., Clark, I., Grant, M., and Braun, R., "High Mass Mars Entry, Descent, and Landing Architecture Assessment," AIAA 2009-6684, AIAA Space 2009 Conference and Exposition, Pasadena, CA, 14-17 Sept. 2009.

[5] Mendeck, G. F. and Craig, L. E., "Entry Guidance for the 2011 Mars Science Laboratory mission," AIAA 2011-6639, Portland, OR, Aug. 2011.

[6] Açikmeşe, B., and Ploen, S., "Convex Programming Approach to Powered Descent Guidance for Mars Landing," Journal of Guidance, Control, and Dynamics, Vol. 30, No. 5, pp. 1353-1366, 2007.

[7] Wolf, A.A.; Tooley, J.; Ploen, S.; Ivanov, M.; Acikmese, B.; Gromov, K., "Performance Trades for Mars pinpoint Landing," *IEEE Aerospace Conference, 2006.*

[8] Steinfeldt, B.A.; Grant, M.J.; Matz, D.A.; Braun, R.D.; and Barton, G.; "Guidance Navigation and Control System Performance Trades for Mars Pinpoint Landing," *Journal of Spacecraft and Rockets*, Vol. 47, No. 1, pp. 188-198, Jan-Feb, 2010.

[9] Meginnis, I.M.; Putnam, Z.R.; Clark, I.G.; Braun, R.D.; and Barton, G.H.; "Guided Entry Performance of Low Ballistic Coefficient Vehicles at Mars," *Journal of Spacecraft and Rockets*, Vol. 50, No. 5, pp. 1047-1059, Sept-Oct, 2013.

[10] Grant, M.J., et al., "Smart Divert: A New Mars Robotic Entry, Descent, and Landing Architecture," *Journal of Spacecraft and Rockets*, Vol. 47, pp. 385-393, May-June 2010.

[11] H. L. Justh and H. S. Ramey, "MARS-GRAM 2010: IMPROVING THE PRECISION OF MARSGRAM,"
4th InternationalWorkshop on the Mars Atmosphere: Modelling and Observations, Feb. 2011,
pp. 1–4.

[12] Cruz, J.R., et al., "Parachute Models Used in the Mars Science Laboratory Entry, Descent, and Landing Simulation," AIAA 2013-1276, 2013 AIAA Aerodynamic Decelerator Systems Conference, March 2013.

[13] Putnam, Z.R. and Braun, R.D.; "Precision Landing at Mars Using Discrete-event Drag Modulation," AAS-13-438, 23rd AAS/AIAA Spaceflight Mechanics Meeting, Kauai, HI, February 2013.

[14] Prakash, R., Burkhart, P. D., Chen, A., *et al.* "Mars Science Laboratory Entry, Descent, and Landing System Overview". 2008 IEEE Aerospace Conference. Big Sky, Montana. pp. 1–18.

[15] Clark, I.M., Hutchings, A.L., Tanner, C.L., and Braun, R.D. "Supersonic Inflatable Aerodynamic Decelerators for Use on Future Robotic Missions to Mars," *Journal of Spacecraft and Rockets*, Vol. 46, No. 2, pp. 340-352, Mar-Apr, 2009.

[16] Korzun, A.M., Braun, R.D., "Performance Characterization of Supersonic Retropropulsion for High-Mass Mars Entry Systems," *Journal of Spacecraft and Rockets*, Vol. 47, No. 5, pp. 836-848, Sep.-Oct., 2010.

[17] Marsh, C.L. and Braun, R.D.; "Fully Propulsive Mars Atmospheric Transit Strategies for High-Mass Missions," *Journal of Spacecraft and Rockets*, Vol. 48, No. 2, pp. 271-282, Mar-Apr, 2011.

[18] Wolf, A., Ivanov, M., "SuperSmart Parachute Deployment Algorithm for Mars Pinpoint Landing," AIAA/AAS Astrodynamics Specialist Conference and Exhibit, 2008.

[19] Prakash, R., Burkhart, P. D., Chen, A., *et al.* "Mars Science Laboratory Entry, Descent, and Landing System Overview". 2008 IEEE Aerospace Conference. Big Sky, Montana. pp. 1–18.